624 *Chem. Mater.* **2010,** *22,* 624–634
DOI:10.1021/cm901956r

CHEMISTRY OF MATERIALS
Review

Zintl Chemistry for Designing High Efficiency Thermoelectric Materials[†,‡]

Eric S. Toberer,[§] Andrew F. May,[∥] and G. Jeffrey Snyder*[,§]

[§]*Materials Science, California Institute of Technology, Pasadena, California 91125, and* [∥]*Chemical Engineering, California Institute of Technology, Pasadena, California 91125*

Received July 2, 2009. Revised Manuscript Received September 23, 2009

Zintl phases and related compounds are promising thermoelectric materials; for instance, high zT has been found in $Yb_{14}MnSb_{11}$, clathrates, and the filled skutterudites. The rich solid-state chemistry of Zintl phases enables numerous possibilities for chemical substitutions and structural modifications that allow the fundamental transport parameters (carrier concentration, mobility, effective mass, and lattice thermal conductivity) to be modified for improved thermoelectric performance. For example, free carrier concentration is determined by the valence imbalance using Zintl chemistry, thereby enabling the rational optimization of zT. The low thermal conductivity values obtained in Zintl thermoelectrics arise from a diverse range of sources, including point defect scattering and the low velocity of optical phonon modes. Despite their complex structures and chemistry, the transport properties of many modern thermoelectrics can be understood using traditional models for heavily doped semiconductors.

Introduction

The solution to the current energy dilemma rests on a concerted effort to broaden our energy resources (solar, wind, biofuels, etc.) and reduce our energy consumption. More than half the energy consumed nationwide is lost as heat, and the recovery of even a small fraction would significantly impact global energy use.[1] A new energy landscape could thus include thermoelectric materials to produce electricity through waste heat recovery or cogeneration. Thermoelectric refrigeration also offers an alternative to compression-based refrigeration that employs atmospheric pollutants.[2,3]

Like all heat engines, the power generation efficiency (η) of a thermoelectric device is thermodynamically limited by the Carnot efficiency. Thermoelectric materials are far from ideal, leading to an additional material factor, zT. The device efficiency κgenerally increases with increasing zT.[4]

$$zT = \alpha^2\sigma T/\kappa \tag{1}$$

The material figure of merit, zT, depends on the Seebeck coefficient (α), temperature (T), electrical conductivity (σ), and thermal conductivity (κ). The Seebeck coefficient characterizes the voltage generated due to a temperature gradient ($\alpha = \Delta V/\Delta T$ for small ΔT). Traditional thermoelectric materials have zT near unity; however, there has been an increasing number of reports of larger zT values through enhancements in both electronic and thermal properties.[4−14]

A material with a large zT needs to have a large Seebeck coefficient (found in low carrier concentration semiconductors or insulators) and a large electrical conductivity (found in high carrier concentration metals). The carrier concentration (n) dependence of these properties is shown in eqs 2 and 3. In these equations, m^* is the density of states effective mass, μ is the charge carrier mobility, and eq 2 is generally valid for a single parabolic band at high n and/or low T.

$$\alpha = \frac{8\pi^2 k_B^2}{3eh^2} m^* T \left(\frac{\pi}{3n}\right)^{2/3} \tag{2}$$

$$\sigma = ne\mu \tag{3}$$

As a consequence of the balance between the Seebeck coefficient and electrical conductivity, most good thermoelectric materials are heavily doped semiconductors. These materials typically possess carrier concentrations of $10^{19}-10^{21}$ carriers/cm^3. Thermoelectric optimization is additionally complicated by thermal transport, which occurs by both electrons and phonons. The compromise in transport properties[4] is illustrated in Figure 1.

To ensure that the net Seebeck coefficient is large, one charge carrier should dominate transport. Mixed n-type and p-type conduction reduces the overall voltage from a temperature gradient as both electrons and holes move to the cold end. Most good thermoelectric materials therefore have the Fermi level near the edge of a band gap. Materials with band gaps can usually be understood as valence compounds using the general valence rule discussed below. In an ionic compound, the stoichiometric sum of the formal ionic valencies exactly balance, leading

[†] Accepted as part of the 2010 "Materials Chemistry of Energy Conversion Special Issue".
[‡] Dedicated to Prof. Arndt Simon on the occasion of his 70th birthday.
*E-mail: jsnyder@caltech.edu.

 Published on Web 11/09/2009

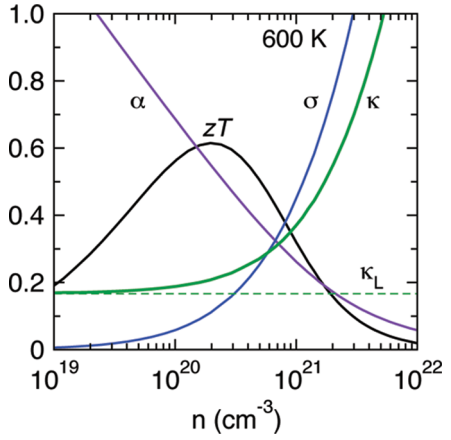

Figure 1. Dependence of thermoelectric properties on carrier concentration (n) expected for a classic semiconductor.[4] Curves are based on results from a $Ba_8Ga_{16-x}Ge_{30+x}$ sample with $n = 8 \times 10^{20}$ cm^{-3} at 600 K generated with a single parabolic band model. The value of 1 on the y-axis corresponds to $zT = 1$; $\alpha = 400\,\mu$V/K; $\sigma = 2 \times 10^5$ S/m; $\kappa = 5$ W/(m K).

to noble gas electron configurations. The band gap occurs between filled anionic states (valence band) and empty cationic states (conduction band). Covalently bonded semiconductors arise when a band gap is formed between filled bonding and unoccupied antibonding electronic states. The formal valencies in covalent semiconductors balance when the number of covalent bonds and contributed valence electrons are taken into account. The general valence method works by comparing the number of electronic states in the valence band with available electrons rather than by assuming complete charge transfer.[15]

Frequently, complex materials can be understood using the Zintl−Klemm approach to valence counting.[13,15−18] In Zintl phases, the formal valence of atoms can be assigned using relatively simple rules that allow a variety of cation and anion types originating from ionic, covalent, and metal−metal bonding. The strict definition of a Zintl phase requires them to be valence balanced and semiconducting ($E_g > 0$, Figure 2a).[17,18] Many qcompounds are valence balanced according to the Zintl counting formalism but are metallic (or more correctly semimetallic) rather than semiconducting because the valence and conduction bands overlap ($E_g < 0$) (Figure 2b). Semimetals are rarely good thermoelectrics because of the coexistance of electrons and holes.[19]

Many good thermoelectric materials are structurally related to Zintl phases, although they do not comply with the strict definition of Zintl phases as intrinsic semiconductors.[13,17] This is because good thermoelectrics have the Fermi level inside a band but near a band gap, giving them the transport properties of a metal at low temperatures (Figure 2c). Such electron rich or poor compounds near an otherwise semiconducting Zintl phase composition have been described as "Zintl metals" or polar intermetallics.[15,18] Despite these materials not being Zintl phases, a detailed understanding of Zintl chemistry can explain many of the structural aspects and transport properties observed in these quite complex materials.

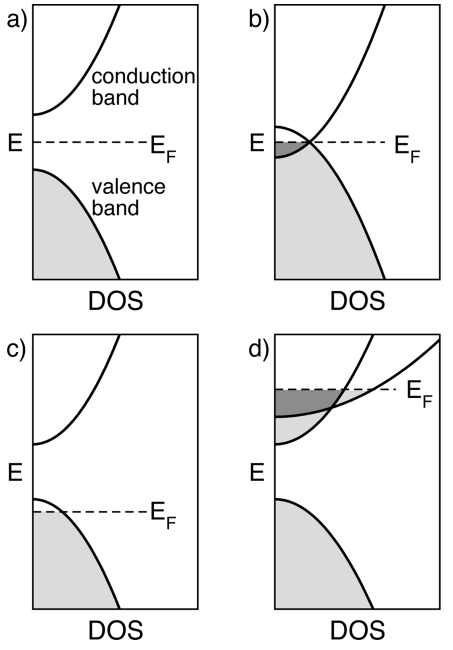

Figure 2. (a) Schematic diagram of the density of states (DOS) of a valence balanced semiconductor. The Fermi level lies in the band gap between the filled valence band and empty conduction band. (b) In a semimetal, band overlap produces metallic behavior despite appearing valence balanced. (c) The Fermi level is displaced from the band gap into a band by the removal of electrons due to a valence imbalance. (d) Multiple conduction bands with different energy minima in La_3Te_4 lead to a larger effective mass when the Fermi level intersects both bands.

This review begins with the success of Zintl chemistry in describing the relationship between the increasing amount of *valence imbalance* (a nonzero stoichiometric sum of the valences) and the observed transition from semiconducting to metallic behavior. The formal valence of a cation, following the general valence rule,[20] is given by eq 4a, where e_c is the number of available valence electrons of the element and b_c is the number of cation−cation two electron bonds and nonbonding lone pair electrons. Similarly, the anion formal valence is given by eq 4b, where b_a is the number of anion−anion two electron bonds. Cation−cation two electron bonds are found in the Mo−Mo interactions within Mo_3Sb_7,[21] and nonbonding lone pair electrons are required to yield valence balance in PbTe.[20]

$$V_c = e_c - b_c \tag{4a}$$

$$V_a = e_a + b_a - 8 \tag{4b}$$

The stoichiometric sum of V_c and V_a is zero for valence compounds such as Zintl phases. Materials that can be understood by Zintl chemistry but may have a valence imbalance are herein referred to as Zintl compounds.

The Zintl compounds discussed in this review are good thermoelectrics because they combine the favorable features of chemical tunability found in intermetallics and the simple electron counting rules associated with valence compounds. The diversity of bonding and structural units frequently leads to complex structures that possess extremely low κ_L. Some of the most intensely studied Zintl compounds for thermoelectrics

are the clathrates[22−25] (e.g. $Ba_8Ga_{16}Ge_{30}$), filled skutterudites (e.g. $Ce_xCo_{4-y}Fe_ySb_{12}$),[26−28] $Yb_{14}MnSb_{11}$,[29−33] and AZn_2Sb_2.[34−37] The important results on these and related materials are well-described in a number of reviews,[5,6,13] including the one by Kleinke in this issue.[21] This review focuses on the chemical methods used to modify electrical and thermal transport in compounds which can be understood using Zintl chemistry.

Carrier Concentration

Chemical control of carrier concentration (n) is the first, and arguably the most important, step in the optimization of thermoelectric efficiency. The control of extrinsic carrier concentration utilizes a valence imbalance achieved by changing the elemental ratio or alloying with additional elements. Defects and impurities in semiconductors, which can arise from processing air sensitive and/or volatile materials, can lead to extrinsic carrier concentrations near 10^{18} cm^{-3}. However, most thermoelectric materials optimize at 10^{19} cm^{-3} $< n <$ 10^{21} cm^{-3}, high enough that n can often be controlled by chemical composition with traditional bulk preparation techniques. The following subsections explore the use of vacancies and alloying to control the carrier concentration by valence imbalance in several model compounds.

We have found that the free electron concentration, as observed by Hall effect measurements, frequently corresponds to that expected from the stoichiometric sum of V_c and V_a (valence imbalance). This was demonstrated[38] for $La_{3-x}Te_4$ and shown in Figure 3 for $Ba_8Ga_{16-x}Ge_{30+x}$ and $Yb_{14}Al_{1-x}Mn_xSb_{11}$, where the dashed lines are obtained from the valence imbalance and volume per formula unit.

In the search for or optimization of new thermoelectric materials, one can start with a valence balanced composition (e.g., $Ba_8Ga_{16}Ge_{30}$) and substitute elements of a different formal valence to quantitatively change n in a predictive manner. Alternatively, one can start with an extremely electron rich or electron poor Zintl compound (e.g., $Yb_{14}MnSb_{11}$)[29,30] and tune the composition toward a valence balanced state, provided a band gap exists (not a semimetal).

Some Zintl compounds, such as the clathrates, allow both n- and p-type compositions to be achieved.[39] Making thermoelectric couples out of such material pairs is appealing due to the similar physical properties. Unfortunately, many Zintl compounds appear to favor a particular carrier type. For example, in $Yb_{14}AlSb_{11}$ and LiZnSb, only p-type compositions have be formed; likewise $La_{3-x}Te_4$ has only formed n-type.[30,38,40] Limited carrier concentration ranges may be due to narrow phase boundaries or competition from other low energy phases.

Cation Vacancies: $La_{3-x}Te_4$. The use of point defects to set the extrinsic carrier concentration has been demonstrated in several traditional thermoelectrics. For instance, in PbTe, the tellurium content may be controlled via Te vapor pressure, thus providing a slight valence imbalance in a nominally valence balanced compound.[41]

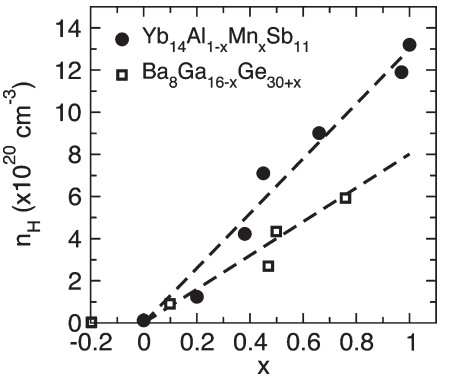

Figure 3. Good agreement is found between experimental Hall carrier concentrations (n_H) and the theoretical curves based on electron counting in p-type $Yb_{14}Al_{1-x}Mn_xSb_{11}$ and n-type $Ba_8Ga_{16-x}Ge_{30+x}$.[23,30]

Cation vacancies have been used to control carrier concentration in the rare earth chalcogenides based on the Th_3P_4 structure.[14,42,43] For example, in lanthanum telluride, a complete solid solution is found between valence imbalanced La_3Te_4, which has the transport properties of a metal, and the vacancy-rich, charge balanced $La_{2\frac{2}{3}}Te_4$ composition (ionic La_2Te_3). In this system, La cations donate electrons to completely fill the Te states; excess electrons partially fill the conduction band, which is composed primarily of La character. The corresponding n-type carrier concentration is consistent with the valence imbalance according to $La_{3-x}{}^{3+}\square_xTe_4{}^{2-} + e_{1-3x}{}^-$.[38] Note that the presence of cation vacancies does not alter the number of states in the valence band but only changes the number of valence electrons added to the system. Synthetically, accessing such a narrow compositional window (3 at % Te phase width) is quite challenging due to the high melting point of $La_{3-x}Te_4$ and the low boiling point of tellurium. High energy ball-milling has proven vital in the controlled synthesis of homogeneous $La_{3-x}Te_4$, as the product is formed directly from the elements near room temperature. Controlling the carrier concentration of $La_{3-x}Te_4$ in this manner allows an optimization of thermoelectric properties, yielding a peak zT of 1.1 at 1275 K. This is an improvement over the prior state-of-the-art $Si_{0.8}Ge_{0.2}$ alloy used on NASA space probes.

Cation Alloying: $Yb_{14}AlSb_{11}$. Along with vacancies, alloying is a common mechanism used to control carrier concentration in semiconductors. In the high temperature thermoelectric material $Si_{0.8}Ge_{0.2}$, boron (with one less valence e$^-$ than Si or Ge) and phosphorus (with one more valence e$^-$) substitutions are used to render the material p- and n-type, respectively. Similar alloying approaches have been shown with Zintl compounds, such as in the charge balanced $Yb_{14}AlSb_{11}$, which has a peak zT of 0.1 at 1250 K. A complete solid solution can be formed by the substitution of Mn^{2+} for Al^{3+} ($Yb_{14}Al_{1-x}Mn_xSb_{11}$), which leads to electron deficiency.[30] The electron deficiency is observed as a linear increase in hole concentration with increasing x and matches the trend expected by simple electron counting (Figure 3). Consequently, the increasing carrier density leads to a simultaneous

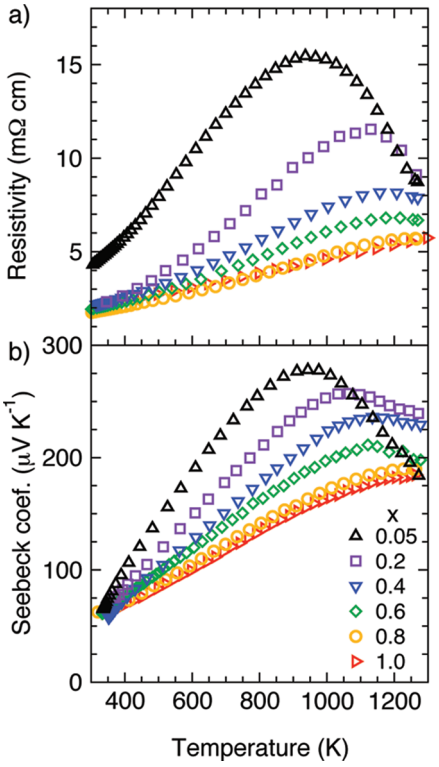

Figure 4. Hole doping in $Yb_{14}Al_{1-x}Mn_xSb_{11}$ is obtained when Mn^{2+} is substituted for Al^{3+}. With increasing valence imbalance (x), the resistivity and Seebeck coefficient decrease, as expected for a heavily doped semiconductor.[30]

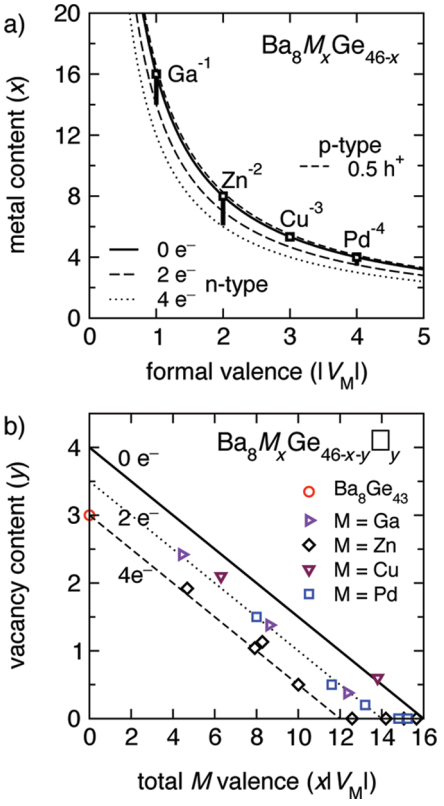

Figure 5. (a) Valence balanced, semiconducting compositions (square symbols) for a variety of M-site species with formal valence V_M in $Ba_8M_xGe_{46-x}$. In Ge-clathrates, the range of stable, vacancy-free compositions (heavy vertical lines in panel a) is found to be no greater than 4 e^-/f.u. (n-type) and ~0.5 h^+/f.u. (p-type). (b) At high e^-/f.u. concentrations, vacancies form and accept free electrons ($Ba_8M_xGe_{46-x-y}\square_y$). The vacancy content rises as the M content decreases, maintaining a similar electron count as found in the maximum vacancy free composition (panel a). For all M, at low x, the electron count should converge to the 4e^-/f.u. limit at $Ba_8Ge_{43}\square_3$.[44−47]

decrease in electrical resistivity and Seebeck coefficient, as shown in Figure 4. A peak zT of 1.1 is obtained by an optimization of the carrier concentration to 4.5×10^{20} cm^{-3} ($Yb_{14}Al_{0.6}Mn_{0.4}Sb_{11}$).[30,33] This order of magnitude difference in thermoelectric performance underscores the need to study extrinsically doped compounds when assessing a material's potential for thermoelectric applications.

A similar optimization of zT has been demonstrated by substituting La^{3+} for Yb^{2+} after replacing Al^{3+} with Mn^{2+} ($Yb_{14-x}La_xMnSb_{11}$).[29] Here, La^{3+} donates an additional electron compared to Yb^{2+} and partially "backfills" the empty valence band states. The availability of two cation species in $Yb_{14}AlSb_{11}$ that can be used to tune carrier concentration is attractive for thermoelectric optimization. In general, complex Zintl compounds contain a variety of sites that allow chemical tuning.

Anion Vacancies and Alloying: $Ba_8Ga_{16-x}Ge_{30+x}$. In the clathrates, which contain covalently bound frameworks surrounding guest atoms, alloying is the primary tool for manipulating carrier concentration, although the formation of vacancies becomes important at large valence imbalance. Valence balanced, semiconducting clathrates can be understood when the guest atoms are treated as nonbonded ions and the framework atoms are assigned formal valencies as defined above for anions (eq 4b).[48] In the type-I clathrate $[Ba^{2+}]_8[Ga^{-1}]_{16-x}[Ge^0]_{30+x}$, each Ge is four bonded (4b), which reduces the anion valence by 1 per bond and yields a formal valence of zero (4b-Ge^0).[49] Since Ga is alloyed with Ge on the framework sites, the formal valence is likewise reduced by four and thus Ga is a monovalent acceptor (4b-Ga^{-1}). Valence balance is thus clearly obtained for $x = 0$. Valence imbalance leads to the presence of free charge carriers, namely electrons and holes for $x > 0$ and $x < 0$, respectively.[39] A number of studies have characterized the thermoelectric properties of n-type $Ba_8Ga_{16-x}Ge_{30-x}$ and peak zT values of ~0.8 at ~950 K are found for polycrystalline material.[23] In contrast, relatively few studies have examined transport in p-type $Ba_8Ga_{16-x}Ge_{30-x}$, and the phase width is found to be narrower[39] than in n-type $Ba_8Ga_{16-x}Ge_{30-x}$ (Figure 5a). Similar adjustments of framework composition have been used to control the carrier concentration in $Ba_8Al_{16-x}Ge_{30-x}$ and $Eu_8Ga_{16-x}Ge_{30-x}$, among others.[50−52] Even the so-called "inverse clathrates", where the guest atom is an anion (such as I^-), follow these valence counting rules with a positive formal valence on the framework.[48,53]

When the valence imbalance due to insufficient acceptors is large, requiring many high energy electrons in the conduction band, a framework vacancy can form despite an energetic penalty arising from the breaking of covalent bonds. For example, the type-I clathrate $K_8Ge_{46-x}\square_x$ should be a charge balanced semiconductor when $x = 2$,

as isolated vacancies act as tetravalent acceptors for the electrons from the eight K^+. Alternatively, we can describe the formation of a vacancy as requiring the breaking of four covalent Ge−Ge bonds, leaving four ($3b$-Ge^{-1}) monovalent acceptors per vacancy. However, $K_8Ge_{46-x}\square_x$ is metallic and n-type, suggesting that $x < 2$ is formed due to an energetic balance between vacancy formation and the intrinsic electronic state.[54,55] Similar behavior is observed with the hypothetical compound $Ba_8Ge_{42}\square_4$, which should be a semiconductor; however, $Ba_8Ge_{43}\square_3$ forms with 4 free e^- per formula unit.[56,57]

The equilibrium between vacancy formation and the filling of antibonding states (conduction band) is also seen in the ternary clathrates $Ba_8M_xGe_{46-x-y}\square_y$.[44−47,58,59] Valence balanced compositions for M = Ga, Zn, Cu, and Pd are located on the solid curve ($x = 16/V_M$, V_M valence of M) in Figure 5a. The phase widths of vacancy free ($y = 0$) compositions are highlighted by the vertical lines and corresponds to approximately 0.5 h^+ to 2 e^-/f.u. (formula unit) for M = Ga. These phase widths are obtained by extrapolating the vacancy-rich compositions shown in Figure 5b to the limit of zero vacancies. While some variation in phase width is observed between different M, collectively the data suggest the energetics between free carrier and vacancy formation balance near 2 e^-/f.u. regardless of M species. When the valence imbalance exceeds this apparent maximum, vacancy formation is observed.

The relationship between vacancy content (y) and extent of valence imbalance ($16 - x|V_M| - 4y$) is shown in Figure 5b. Similar representations of Figure 5b have been shown previously;[46,47] here, we emphasize the importance of valence, rather than metal content, by plotting the total M valence ($x|V_M|$). This reveals that the compositional boundaries in $Ba_8M_xGe_{46-x-y}\square_y$ appear to be determined by a maximum valence imbalance (x-intercept) and simple electron counting rules.

Consider, for example, electron counting and vacancy formation in $Ba_8Zn_xGe_{46-x-y}\square_y$, where Zn acts as a divalent acceptor.[47] $Ba_8Zn_8Ge_{38}$ is a valence balanced semiconductor (Figure 5a). Reducing the Zn content to $Ba_8Zn_6Ge_{40}$ yields a vacancy-free composition which is electron rich (4 e^-/f.u.). For $x < 6$, vacancy formation maintains the carrier concentration near 4 e^-/f.u. as observed in Figure 5b (e.g., $Ba_8Zn_2Ge_{42}\square_2 + 4\,e^-$). These valence counting arguments extend to the Zn-free $Ba_8Ge_{43}\square_3 + 4\,e^-$, described above.

Estimating Optimum Carrier Concentration. The most direct method to optimize a thermoelectric material is to prepare samples with a range of doping levels and characterize their relevant thermoelectric properties, including Hall effect measurements. Such a study can reveal details of the transport not captured by the usual single parabolic band approximation, such as changes in scattering mechanism or multiband effects.[38] However, there are many "potential" thermoelectric materials to investigate and adjusting carrier concentration can be nontrivial. Therefore, an initial screening mechanism is required.

One approach is to estimate the maximum zT and optimal carrier density for a given system based on the properties of an unoptimized sample. The process begins by analyzing transport data at a particular temperature within the confines of the single parabolic band assumption to reveal fundamental material parameters, including the effective mass (m^*), lattice thermal conductivity (κ_L), and mobility at the limit of low doping (μ_o).[23,60,61] Using these fundamental material parameters, the dependence of the thermoelectric transport properties on carrier concentration is computed using the single parabolic band model.

Figure 6 compares the experimental zT obtained for $Ba_8Ga_{16-x}Ge_{30+x}$ ($0 < x < 1$) at 600 K to the predicted zT curve, which is generated using transport data from the highest carrier concentration sample.[23] Despite obtaining the input parameters (m^*, μ_o, κ_L) from the nonoptimal sample with $zT = 0.3$, the optimized carrier concentration and maximum zT (0.5 at 600 K) are in reasonable agreement with the experimental data. As an alternative to the above approach, a graphical method to estimate maximum zT at a particular temperature uses the "quality factor" β.[14,60]

$$\beta = \frac{m^{*3/2}\mu_o}{\kappa_L} \tag{5}$$

Use of the single band model to estimate optimal carrier concentration does, however, come with several requirements and assumptions. The input parameters are only representative when obtained from an extrinsically doped sample. The limiting scattering mechanism for the carrier mobility should be considered; typically acoustic phonon scattering is assumed. The temperature of interest must be low enough that the single carrier type assumption applies (thermal activation of minority carriers is negligible). Unfortunately, the temperature of maximum zT typically occurs when the single carrier type assumption breaks down. Note that Figure 6 is not used at the peak zT temperature (950 K), but rather at 600 K. The major assumption in this approach is that the fundamental material parameters (m^*, μ_o, κ_L) are invariant with composition/doping level. Regardless of these limitations, the single parabolic band model is a powerful tool in the screening and optimization of materials for thermoelectric efficiency.

Mobility and Effective Mass

The electronic component of thermoelectric transport is characterized by two key properties: carrier effective mass (m^*) and mobility (μ). The importance of these parameters in eq 5 leads to frequent use of the "weighted mobility", $m^{*3/2}\mu$. In the classical approximation, carrier mobility is determined by the carrier's inertial effective mass (m_i^*) and the time between scattering events (τ), eq 6.

$$\mu = \tau e/m_i^* \tag{6}$$

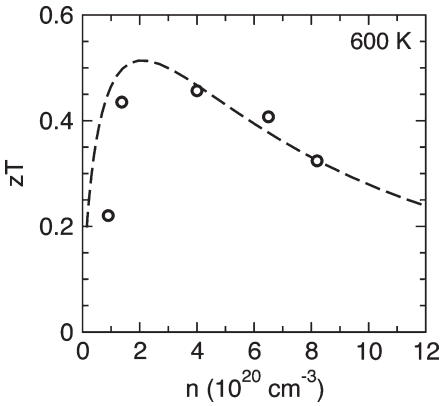

Figure 6. $Ba_8Ga_{16-x}Ge_{30+x}$ ($0 < x < 1$) zT values at 600 K, and the corresponding prediction using the single band approximation with data from the 8×10^{20} cm^{-3} sample.[23]

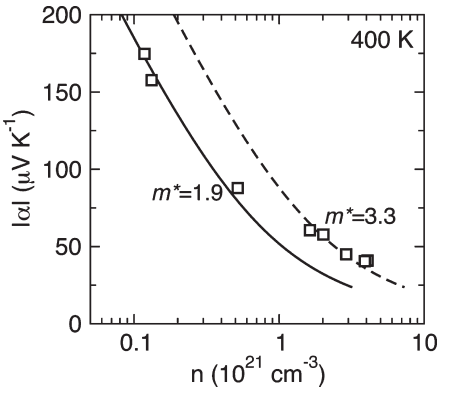

Figure 7. Pisarenko plot showing experimental Seebeck coefficients for $La_{3-x}Te_4$ and the predicted single parabolic band behavior for m^*/m_e = 1.9, 3.3. Two different curves are required to described the data due to multiple band effects in $La_{3-x}Te_4$.[89]

Heavy carriers have low group velocity and therefore generally have low mobility. Charge carriers face a number of scattering sources that reduce mobility, including lattice vibrations, ionized impurities, nonionized crystal defects, extended defects, grain boundaries, and even disordered spin states.

The inertial effective mass is related to the density of states effective mass (m^*), which is a key factor in determining the magnitude of the Seebeck coefficient for a given carrier density (eq 2). To first order, high μ and large m^* are conflicting, and thus, a large weighted mobility is difficult to obtain.[14]

In classic binary semiconductors, high mobility and low effective mass are frequently found in materials with small differences in electronegativity (e.g. $IrSb_3$ μ = 1320 $cm^2/(V\ s)$, m^*/m_e = 0.17 at 300 K) while low mobility and high effective mass are found in ionic materials (e.g. $Fe_xCr_{3-x}Se_4$ μ = 0.1 $cm^2/(V\ s)$, m^*/m_e = 4 at 300 K).[8,43,62,63] Zintl compounds, which frequently exhibit both ionic and covalent bonding, bridge these extremes. For instance, metallic $YbZn_2Sb_2$ and $Yb_{14}MnSb_{11}$ have μ of 130 and 3 $cm^2/(V\ s)$ at 300 K, respectively.[30,34] In general, the large variation in μ for Zintl compounds is due to changes in both m^* and τ.

Electronic Transport Analysis. Investigating the dependence of mobility and effective mass on carrier concentration and/or chemical modification is one of the best methods to examine a material's "effective" band structure. Through analysis of the Seebeck coefficient and Hall effect data, a density of states effective mass is obtained for a given doping level and temperature assuming a single parabolic band electronic structure. If similar m^* values are obtained at a variety of n, one can generally conclude that transport is well-described by a single parabolic band model. Another way to visualize the dependence of m^* on n is the Pisarenko plot, which shows α as a function of n (Figure 7). The effect of chemical dopants on m^* can be clearly visualized in a Pisarenko plot, where deviations from the baseline curve are readily observed if m^* changes. For example, Tl doping of PbTe increases the hole effective mass compared to a Na−PbTe baseline and, despite a concurrent decrease in mobility, an increase in thermoelectric efficiency was observed.[12]

Parabolic Band: *n*-Type $Ba_8Ga_{16-x}Ge_{30+x}$. In *n*-type $Ba_8Ga_{16-x}Ge_{30+x}$, the effective mass is constant with carrier concentration in the region of high zT, suggesting that the relevant band structure is parabolic.[23,64] Computational studies have revealed the minimum energy conduction band is nearly parabolic and formed via hybridization of guest atom bonding and framework antibonding orbitals.[65]

There has been significant interest in the relationship between conduction band mass and chemical composition, and the roles of filler and framework species have been investigated.[65−75] Transition metal substitution in $Ba_8M_yGa_xGe_{46-x-y}$, for example, can lead to enhancement of m^* but can also reduce mobility (eq 7) and band gap.[64,76] Experimental and computational studies of Ni, Au, Pd, and Pt substitution have found effective mass values up to twice that found in $Ba_8Ga_xGe_{46-x}$ (m^* values are tabulated in ref 66).[66,77,78]

Changes in mobility can be due to the role of microstructure and point defects, as well as changes in band structure. For example, copper substitution in nominally valence balanced $Ba_8Cu_xGa_{16-3x}Ge_{30+2x}$ revealed an enhancement in mobility with increasing copper content. This was attributed to a reduction in alloy scattering associated with a preferential site occupation for Cu and increased Ge content, rather than a decrease in effective mass.[24,79,80] Cu substitution has also been investigated without charge balancing ($Ba_8Cu_xGe_{46-x}$),[81] and no increase in mobility was observed, possibly due to the formation of vacancies.

Nonparabolic Band: Skutterudites. In the filled skutterudites, *n*-type conduction can be obtained by filling the cages of valence balanced $CoSb_3$ with electron donating cations (e.g. $[R]_x[Co^{3+}][Sb^{-1}]_3$, R = Nd, Tl, Ba, La, Ce, Yb, Sr). Through such chemical modifications, it has been revealed that the effective mass increases with increasing carrier concentration. In this case, the band structure is close to linear and is well-described by the Kane model for nonparabolic bands.[82−84] The relationship between m^* and n is not affected by choice of filler

atom R, implying the conduction band edge is similar across these filled skutterudites.[84−86] Similar quasilinear behavior is found in the p-type skutterudite $La(Fe_{0.75}Co_{0.25})_3Sb_{12}$.[87,88]

Multiple Bands: $La_{3-x}Te_4$. Density functional theory calculations reveal the conduction band edge of $La_{3-x}Te_4$ is described by multiple bands; a light (small m^*) conduction band extends to the band gap while heavy bands are present at slightly higher energies.[89] Figure 2d represents this band structure when transport is determined by both the light and heavy bands. At lower E_F, corresponding to lower carrier concentration, the 'effective' mass of the carriers is reduced due to transport in the light band. The Pisarenko plot for $La_{3-x}Te_4$ (Figure 7) demonstrates this multiband feature by comparing the experimental data to two single band models (assuming acoustic scattering limits μ), where the low n data are better described by the model with smaller m^*.

Complex Zintl Phases: $Yb_{14}Al_{1-x}Mn_xSb_{11}$. Of the thermoelectric materials with high zT, $Yb_{14}Al_{1-x}Mn_xSb_{11}$ possesses one of the most complex crystal structures, with spin-dependent and anisotropic thermoelectric transport properties. Despite this complexity, initial analysis found a single parabolic band model provides a reasonable description of the transport for $x \geq 0.2$.[30] The carrier mobility at room temperature was well-described by the theory of acoustic phonon scattering, which predicts $\mu \propto n^{-1/3}$ for high doping levels.[61]

Given the complexity of $Yb_{14}Al_{1-x}Mn_xSb_{11}$, many opportunities exist for enhancement beyond those associated with carrier concentration optimization. In particular, eliminating sources of carrier scattering which reduce mobility and provide no benefit to α or κ_L is desirable. Initial efforts in this regard focused on the role of magnetoresistance in $Yb_{14}MnSb_{11}$, which at high temperature is observed as a residual resistance.[90,91] This magnetoresistance has been shown to primarily arise from the disordered d^5 Mn^{2+} spin states. In the analogous $Yb_{14}ZnSb_{11}$, magnetoresistance is greatly reduced due to the presence of nonmagnetic d^{10} Zn^{2+}. Thus substitution of Zn for Mn removed magnetic scattering in $Yb_{14}Mn_{1-x}Zn_xSb_{11}$ and a linear decrease in the residual resistance was observed with increasing x (for $x \leq 0.8$), leading to a ~10% increase in maximum zT.[31]

Electronic Structure Calculations

Electronic structure calculations can facilitate the selection and optimization of thermoelectric materials.[92,93] These calculations typically adopt a rigid band approach, where a single calculation of the band structure is performed and the Fermi level is subsequently varied to mimic various doping levels. The Seebeck coefficient and electrical conductivity may be calculated from the relevant Boltzmann transport equations. However, these calculations require assumptions about the dominant scattering mechanism and the magnitude of the carrier relaxation time τ. A common approximation is that τ is independent of carrier energy, contrary to the commonly observed energy-dependent scattering in thermoelectric materials. However, in calculations of the Seebeck coefficient using the energy-independent approximation, the magnitude of τ divides out and reasonable values of α can be obtained. Calculations of σ and κ_e can be less accurate because they depend on the magnitude of τ. Other challenges include determining κ_L and proper treatment of f-electrons in compounds containing rare earth elements.

Several candidate high zT antimonides have been identified from automated searches of thermoelectric performance, most notably LiZnSb with a predicted zT of ~2 when doped n-type.[92] Experimentally, p-type LiZnSb is found to have values of τ and κ_L which are similar to the assumptions used in the calculations.[40] Unfortunately, efforts to form an n-type composition have been unsuccessful. As electronic structure calculations for thermoelectric behavior continue to improve, these surveys will likely become increasingly valuable for research into thermoelectrics.

Thermal Conductivity

Thermal conductivity is the sum of electronic and phonon (lattice vibrations) contributions: $\kappa = \kappa_e + \kappa_L$. The electronic term is usually proportional to the electrical conductivity and can be estimated from the Wiedemann−Franz relationship ($\kappa_e = L\sigma T$) with the Lorenz number (L) approximated as the metallic limit or calculated from Boltzmann transport theory. While κ_e is effectively tied to the numerator in zT, many routes exist to independently modify κ_L.[4,6,94]

We begin by considering what determines κ_L in a crystal at high temperature. Heat is transported by phonons, which have group velocities (v_g) and mean free path lengths (l) between scattering events. The amount of heat transported is proportional to the heat capacity (C_v). Traditionally, the phonon velocity is approximated by the mean sound velocity v, giving a lattice thermal conductivity shown in eq 7 by analogy with the kinetic theory of gases.

$$\kappa_L = \frac{1}{3} C_v v l \tag{7}$$

The situation is complicated by the broad spectrum of phonon frequencies present. High energy, optical phonons do not have sufficiently high group velocities to transport an appreciable quantity of heat and thus thermal transport is frequently dictated by the longer wavelength acoustic phonons. The most significant phonon scattering at high temperature is usually phonon−phonon scattering, which gives the $1/T$ dependence of κ_L found in many crystalline materials.

There is much excitement in the thermoelectrics community to design or discover materials with extremely low κ_L.[4] Much of this work has focused on forming nanostructured materials to increase phonon scattering at interfaces.[6,11,94,95] In Zintl compounds, much of the focus has been on obtaining low thermal conductivity through

the mechanisms discussed below: (a) point defect scattering, (b) rattling atoms, and (c) large cell volumes.

Point Defect Scattering. A variety of crystal imperfections, such as vacancies, interstitial atoms, and site substitution, fall under the category of point defects. Point defects reduce lattice thermal conductivity by scattering phonons due to either mass contrast or local strain induced by the defect. The theory developed by Klemens and Callaway for point defect scattering has been successfully applied to thermal transport in a variety of thermoelectric materials.[96−99] In the partially filled skutterudites, $La_{3-x}Te_4$, and in some clathrates, randomly distributed vacancies play a significant role in scattering phonons.[38,53,100,101] It is somewhat remarkable that the thermal transport in the $Ce_yFe_{4-x}Co_xSb_{12}$ skutterudites, where a variety of scattering mechanisms are present, fits well to a model based solely on mass contrast between the vacancy and filler atom.[100]

In Zintl compounds, alloying has been used to induce mass/strain scattering. For example, complete solid solutions based on $YbZn_2Sb_2$ have been formed between the isoelectronic pairs of Yb−Ca, Zn−Cd and Zn−Mn.[34,36,37] In all cases, the lattice thermal conductivity at room temperature is approximately halved due to the mass disorder. Figure 8 shows these results and the predicted reduction in the lattice thermal conductivity of $Yb_{1-x}Ca_xZn_2Sb_2$ using a point defect scattering theory.[96−99,102] Note, however, at high temperatures the reduction in κ_L from phonon−phonon scattering is comparable to the reduction from point defect scattering (lower curve in Figure 8).

Rattling Atoms. In the clathrates and partially filled skutterudites, the low thermal conductivity has been rationalized in terms of the "rattling" motion of an atom within a cage that is slightly too large.[22,26,27] The initial evidence for rattling came from large atomic displacement parameters of the filler atom when analyzed by diffraction techniques. These independent rattling atoms were then believed to act as sources of phonon scattering, leading to low κ_L.[103] Recent work has indicated that in both the clathrates and skutterudites the vibrational modes of the rattling atom are *not* entirely independent of the framework vibrations.[25,104]

In the skutterudites, neutron spectroscopy experiments have revealed strong resonant coupling between the guest atoms and the framework. This work found much of the phonon phase space has low group velocity, reducing their effectiveness for heat transport.[104] Using the results of ultrafast time-resolved optical measurements, good agreement is found between the experimental κ_L and models for the phonon relaxation time which include the effect of phonon resonant scattering.[105] One important realization is that these resonant scattering centers are tuned to a particular spectrum of phonons. For example, the calculated resonant frequency of Yb in $CoSb_3$ is approximately twice that of Ba.[106] This allows phonons with a broad range of frequencies to be scattered by alloying the guest site with elements possessing different resonant frequencies.[86,105,107]

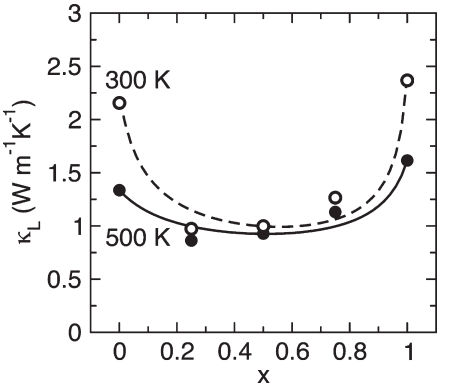

Figure 8. Significant reduction in lattice thermal conductivity is observed due to point defect scattering in $Yb_{1-x}Ca_xZn_2Sb_2$ at 300 and 500 K.[34] Lines show predicted reduction in κ_L based on mass contrast between Yb and Ca for the respective temperatures.[102]

In the clathrates, many sources for low κ_L have been proposed.[24,25,108,109] One explanation comes from neutron triple-axis spectroscopy, which is used to probe the phonon dispersion relation.[25] This work found coupling between the guest atom and the framework leads to low phonon group velocities and thus low κ_L.

The studies of phonons in "rattling" systems suggest that low κ_L results primarily from large unit cells which confine the heat-carrying acoustic phonons to a small fraction of the vibrational states. The following section finds similar conclusions in systems with no apparent rattling species.

Intrinsically Low κ_L: Large Cell Volume. Several Zintl compounds, such as $Yb_{14}MnSb_{11}$, $Yb_{11}GaSb_9$, and $Yb_{11}Sb_{10}$, have extremely low (<1 W/mK) lattice thermal conductivities without evidence for alloying, nanostructuring, or large atomic displacement parameters.[19,30,110] These intrinsically low κ_L materials all possess large unit cells and complex crystal structures. Quantifying the effect of complex bonding and chemical interactions on lattice thermal conductivity is challenging. However, the role of the primitive unit cell volume (V) is more clearly defined, as V dictates the number of phonon states within the first Brillouin zone.

All crystals have $3N$ vibrational modes due to the three degrees of vibrational freedom per atom, where N is the number of atoms per primitive cell. With more than one atom in the unit cell, vibrations with wavelengths shorter than the unit cell (optical modes) are permitted. The $3N$ modes are thus divided between three acoustic modes and $3(N-1)$ optical modes. While each optical mode has the same heat capacity as an acoustic mode, they have low v_g which greatly reduces their contribution to κ_L. The total heat capacity is divided among the modes such that the heat capacity of the acoustic modes is C_v/N. When thermal transport is dominated by acoustic phonons, perhaps the more appropriate mean free path to consider is given by: $\kappa_L \approx \kappa_{L,ac} = {}^1/_3 C_v v l/N$. The high temperature value for the heat capacity is approximately given by the Dulong−Petit relation as $C_v = 3Nk_B/V$, leading to eq 8.

$$\kappa_L \approx k_B v l / V \tag{8}$$

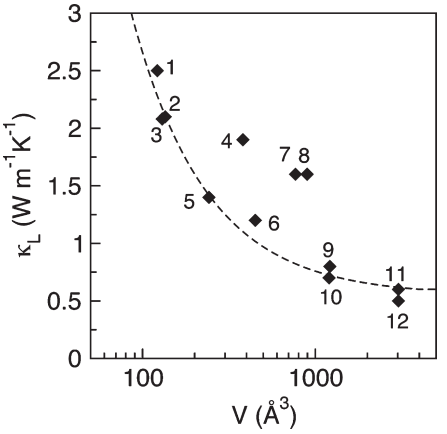

Figure 9. Lattice thermal conductivity at 300 K for a variety of Zintl antimonides assuming a free electron Lorenz number. The dashed line shows the inverse dependence on primitive cell volume, revealing low lattice thermal conductivity at large unit cell volumes: 1-LiZnSb, [92] 2-$SrZn_2Sb_2$,[117] 3-Mg_3Sb_2,[118] 4-$CeFe_4Sb_{12}$,[4] 5-$BaZn_2Sb_2$,[119] 6-$SrZnSb_2$,[117] 7-$Yb_5In_2Sb_6$,[120] 8-$Ba_4In_8Sb_{16}$,[121] 9-$Yb_{11}Sb_{10}$,[19] 10-$Yb_{11}GaSb_9$,[110] 11-$Yb_{14}AlSb_{11}$,[33] 12-$Yb_{14}MnSb_{11}$.[33]

Figure 9 shows the relationship between κ_L and V for a variety of Zintl antimonides (300 K). The dashed line corresponds to a fit to $\kappa_L = aV^{-1} + \kappa_{min}$. Nonzero lattice thermal conductivity is expected even at the glassy limit ($V = \infty$), leading to the inclusion of the κ_{min} term. The remarkable agreement between the experimental κ_L and this simple model is due to the similar chemistry (leading to similar v) and high mass contrast in these compounds. Large mass contrast reduces the role of optical vibrations in the transport of heat.[111]

While differences in v_g and l will cause some variation in κ_L, we generally expect Zintl antimonides with primitive cell volumes ≥ 1000 Å to possess $\kappa_L < 1$ W/mK at 300 K. Similarly low thermal conductivity values are observed in the complex Zintl tellurides with large unit cells.[112−116] Although compounds with large V are attractive for obtaining low κ_L, small unit cells are able to reach similarly low values when other scattering mechanisms are present (e.g. alloy scattering, discussed above for $Yb_{1-x}Ca_xZn_2Sb_2$).

Case Example: Sr−Zn−Sb. The Zintl compounds $SrZnSb_2$ and $SrZn_2Sb_2$ provide a good system to examine the relationship between structure and thermal transport.[117] Similar bonding exists within these compounds (Figure 10), where Zn−Sb covalently bound slabs are separated by monolayers of Sr cations. Speed of sound measurements find essentially identical v at 300 K, as expected from the similarity in bonding. Despite the similarities, $SrZnSb_2$ exhibits significantly lower κ_L than $SrZn_2Sb_2$ near room temperature (Figure 10c). These κ_L results can be attributed to differences in primitive unit cell volume ($SrZnSb_2$ 449.2 Å^3; $SrZn_2Sb_2$ 135.3 Å^3). A more advanced model by Slack,[111] utilizing the number of atoms in the primitive cell, is found to arrive at a similar conclusion.[117]

In addition to differences in unit cell volume, fundamental differences in the two structures could lead to different phonon mean free paths (l). While there is little

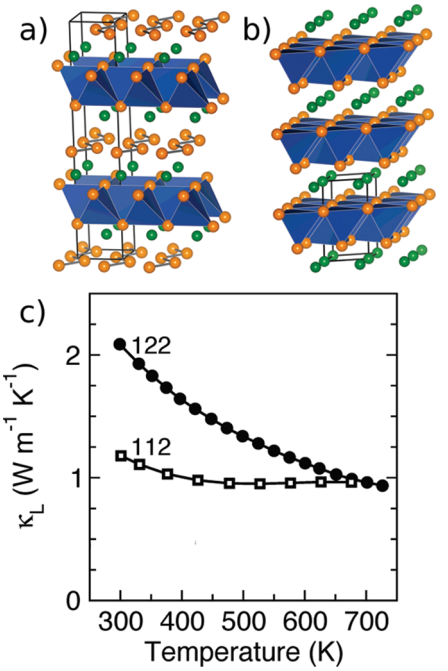

Figure 10. Structures and primitive unit cells of (a) $SrZnSb_2$ (*Pnma*) and (b) $SrZn_2Sb_2$ ($P\bar{3}m$) are both composed of monolayers of Sr (green) and covalently bound slabs of Zn−Sb (blue polyhedra). In $SrZnSb_2$, these layers are alternated with Sb zigzag chains (orange). (c) The more structurally complex $SrZnSb_2$ has a lower lattice thermal conductivity that the chemically similar, yet simpler, $SrZn_2Sb_2$.[117]

room for structural disorder beyond point defects in $SrZn_2Sb_2$, $SrZnSb_2$ is ripe for disorder. $SrZnSb_2$ forms in an orthorhombic cell where a Peierls distortion forms anionic layers of Sb zigzag chains.[16] As shown in Figure 10, the anionic zigzag chains and Zn−Sb covalently bound slabs are separated from each other by cationic monolayers. There is thus the possibility for stacking faults, twinning, and local disorder of these zigzag chains, as well as the usual point defects.

Summary

While the exploration of Zintl compounds for thermoelectrics is in the early stage, the initial successes (e.g. $Ce_xCo_{4-y}Fe_ySb_{12}$, $Yb_{14}MnSb_{11}$, $Ba_8Ga_{16}Ge_{30}$) demonstrate the potential for these materials. This review has discussed how the transport characteristics can be manipulated through a variety of strategies involving valence counting and Zintl structural chemistry. The valence imbalance often determines the free carrier concentration, thereby enabling the rational optimization of zT. Despite the structural complexity of Zintl compounds, simple models like the single parabolic band are found to provide good descriptions of the electronic transport and can estimate thermoelectric performance from limited experimental data. The low lattice thermal conductivity found in complex structures with large unit cell volumes is generally due to the high fraction of low velocity optical phonon modes. Understanding the coupling between chemical structure and thermoelectric transport, which is critical for the development of high efficiency thermoelectric materials, will benefit from the continued discovery and characterization of Zintl compounds.

Acknowledgment. We thank the Beckman Foundation and the Jet Propulsion Laboratory for support.

References

(1) Energy, Environment Directorate, L.L.N.L. https://publicaffairs.llnl.gov/news/energy/energy.html.
(2) Vining, C. B. *Nat. Mater.* **2009**, *8*, 83–85.
(3) Bell, L. E. *Science* **2008**, *321*, 1457–1461.
(4) Snyder, G. J.; Toberer, E. S. *Nat. Mater.* **2008**, *7*, 105.
(5) Nolas, G. S.; Poon, J.; Kanatzidis, M. *MRS Bull.* **2006**, *31*, 199–205.
(6) Chen, G.; Dresselhaus, M. S.; Dresselhaus, G.; Fleurial, J.-P.; Caillat, T. *Inter. Mater. Rev.* **2003**, *48*, 45–66.
(7) D., M. G. *Solid State Phys.* **1997**, *51*, 81–157.
(8) Hsu, K.; Loo, S.; Guo, F.; Chen, W.; Dyck, J.; Uher, C.; Hogan, T.; Polychroniadis, E.; Kanatzidis, M. *Science* **2004**, *303*, 818–821.
(9) Hochbaum, A. I.; Chen, R.; Delgado, R. D.; Liang, W.; Garnett, E. C.; Najarian, M.; Majumdar, A.; Yang, P. *Nature* **2008**, *451*, 163–U5.
(10) Rhyee, J.-S.; Lee, K. H.; Lee, S. M.; Cho, E.; Il Kim, S.; Lee, E.; Kwon, Y. S.; Shim, J. H.; Kotliar, G. *Nature* **2009**, *459*, 965–968.
(11) Poudel, B.; Hao, Q.; Ma, Y.; Lan, Y.; Minnich, A.; Yu, B.; Yan, X.; Wang, D.; Muto, A.; Vashaee, D.; Chen, X.; Liu, J.; Dresselhaus, M. S.; Chen, G.; Ren, Z. *Science* **2008**, *320*, 634–638.
(12) Heremans, J. P.; Jovovic, V.; Toberer, E. S.; Saramat, A.; Kurosaki, K.; Charoenphakdee, A.; Yamanaka, S.; Snyder, G. J. *Science* **2008**, *321*, 554–557.
(13) Kauzlarich, S. M.; Brown, S. R.; Snyder, G. J. *Dalton Trans.* **2007**, *21*, 2099.
(14) Wood, C. *Rep. Prog. Phys.* **1988**, *51*, 459–539.
(15) Nesper, R. *Prog. Solid State Chem.* **1990**, *20*, 1–45.
(16) Papoian, G. A.; Hoffmann, R. *Angew. Chem., Int. Ed.* **2000**, *39*, 2408–2448.
(17) Sevov, S. C. Zintl phases. In *Intermetallic Compounds, Principles and Practice: Progress*; Westbrook, J. H., Freisher, R. L., Eds.; John Wiley & Sons. Ltd.: Chichester, England, 2002; pp 113−132.
(18) Kauzlarich, S. M. *Chemistry, Structure, and Bonding of Zintl Phases and Ions*; Wiley-VCH: New York, 1996.
(19) Brown, S. R.; Kauzarich, S. M.; Gascoin, F.; Snyder, G. J. *J. Sol. State Chem.* **2007**, *180*, 1414.
(20) Pearson, W. B. *Acta Crystallogr.* **1964**, *17*, 1–15.
(21) Kleinke, H. Chem. Mater., available online Aug 25, 2009, http://dx.doi.org/10.1021/cm901591d.
(22) Nolas, G. S.; Cohn, J. L.; Slack, G. A.; Schujman, S. B. *Appl. Phys. Lett.* **1998**, *73*, 178.
(23) May, A. F.; Toberer, E. S.; Saramat, A.; Snyder, G. *J. Phys. Rev. B*, http://link.aps.org/doi/10.1103/PhysRevB.80.125205.
(24) Christensen, M.; Lock, N.; Overgaard, J.; Iversen, B. B. *J. Am. Chem. Soc.* **2006**, *128*, 15657–15665.
(25) Christensen, M.; Abrahamsen, A. B.; Christensen, N. B.; Juranyi, F.; Andersen, N. H.; Lefmann, K.; Andreasson, J.; Bahl, C. R. H.; Iversen, B. B. *Nat. Mater.* **2008**, *7*, 811–815.
(26) Sales, B. C.; Mandrus, D.; Williams, R. K. *Science* **1996**, *272*, 1325.
(27) Morelli, D. T.; Meisner, G. P. *J. Appl. Phys.* **1995**, *77*, 3777–3781.
(28) Chen, B.; Xu, J.-H.; Uher, C.; Morelli, D. T.; Meisner, G. P.; Fleurial, J.-P.; Caillat, T.; Borshchevsky, A. *Phys. Rev. B* **1997**, *55*, 1476–1480.
(29) Toberer, E. S.; Brown, S. R.; Ikeda, T.; Kauzlarich, S. M.; Snyder, G. J. *Appl. Phys. Lett.* **2008**, *93*, 62110.
(30) Toberer, E. S.; Cox, C. A.; Brown, S. R.; Ikeda, T.; May, A. F.; Kauzlarich, S. M.; Snyder, G. J. *Adv. Funct. Mater.* **2008**, *18*, 2795.
(31) Brown, S. R.; Toberer, E. S.; Ikeda, T.; Cox, C. A.; Gascoin, F.; Kauzlarich, S. M.; Snyder, G. J. *Chem. Mater.* **2008**, *20*, 3412–3419.
(32) Brown, S. R.; Kauzlarich, S. M.; Gascoin, F.; Snyder, G. J. *Chem. Mater.* **2006**, *18*, 1873.
(33) Cox, C. A.; Toberer, E. S.; Levchenko, A. A.; Brown, S. R.; Snyder, G. J.; Navrotsky, A.; Kauzlarich, S. M. *Chem. Mater.* **2009**, *21*, 13541360.
(34) Gascoin, F.; Ottensmann, S.; Stark, D.; Haile, S. M.; Snyder, G. J. *Adv. Funct. Mater.* **2005**, *15*, 1860.
(35) Zhang, H.; Zhao, J.-T.; Grin, Y.; Wang, X.-J.; Tang, M.-B.; Man, Z.-Y.; Chen, H.-H.; Yang, X.-X. *J. Chem. Phys.* **2008**, *129*, 164713.
(36) Wang, X.-J.; Tang, M.-B.; Chen, H.-H.; Yang, X.-X.; Zhao, J.-T.; Burkhardt, U.; Grin, Y. *Appl. Phys. Lett.* **2009**, *94*, 92106.
(37) Yu, C.; Zhu, T. J.; Zhang, S. N.; Zhao, X. B.; He, J.; Su, Z.; Tritt, T. M. *J. Appl. Phys.* **2008**, *104*, 13705.
(38) May, A. F.; Fleurial, J.-P.; Snyder, G. J. *Phys. Rev. B* **2008**, *78*, 125205.
(39) Anno, H.; Hokazono, M.; Kawamura, M.; Nagao, J.; Matsubara, K. Proceedings of the Twenty First International Conference on Thermoelectrics **, 2002**; pp 77−80.
(40) Toberer, E. S.; May, A. F.; Scanlon, C. J.; Snyder, G. J. *J. Appl. Phys.* **2009**, *105*, 063701.
(41) Ravich, Y. I.; Efimova, B. A.; Smirnov, I. A. *Semiconducting Lead Chalcogenides*; Plenum: New York, 1970.
(42) Anno, H.; Hokazono, M.; Kawamura, M.; Nagao, J.; Matsubara, K. Thermoelectric properties of $Ba_8Ga_xGe_{46-x}$ clathrate compounds. *Proceedings of ICT 2002, The Twenty-First International Conference on Thermoelectrics*, Long Beach, CA, Aug 25−29, **2002**; pp 77−80.
(43) Rowe, D. M., Ed. *CRC Handbook of Thermoelectrics*; CRC Press: London, 1995.
(44) Carrillo-Cabrera, W.; Cardoso Gil, R.; Paschen, S.; Grin, Y. *Z. Kristallogr. NCS* **2002**, *217*, 183–185.
(45) Melnychenko-Koblyuk, N.; Grytsiv, A.; Rogl, P.; Schmid, H.; Giester, G. *J. Solid State Chem.* **2009**, *182*, 359.
(46) Melnychenko-Koblyuk, N.; Grytsiv, A.; Rogl, P.; Rotter, M.; Bauer, E.; Durand, G.; Kaldarar, H.; Lackner, R.; Michor, H.; Royanian, E.; Koza, M.; Giester, G. *Phys. Rev. B* **2007**, *76*, 144118.
(47) Alleno, E.; Maillet, G.; Rouleau, O.; Leroy, E.; Godart, C.; Carrillo-Cabrera, W.; Simon, P.; Grin, Y. *Chem. Mater.* **2009**, *21*, 1485149.
(48) Kovnir, K. A.; Shevelkov, A. V. *Russ. Chem. Rev.* **2004**, *73*, 923–938.
(49) Corbett, J. *Chem. Rev* **1985**, *85*, 383–397.
(50) Uemura, T.; Akai, K.; Koga, K.; Tanaka, T.; Kurisu, H.; Yamamoto, S.; Kishimoto, K.; Koyanagi, T.; Matsuura, M. *J. Appl. Phys.* **2008**, *104*, 013702.
(51) Fujita, I.; Kisimoto, K.; Sato, M.; Anno, H.; Koyanagi, T. *J. Appl. Phys.* **2006**, *99*, 093707.
(52) Pacheco, V.; Bentien, A.; Carrillo-Cabrera, W.; Paschen, S.; F. Steglich, a. Y. G. *Phys. Rev. B* **2005**, *71*, 165205.
(53) Zaikina, J. V.; Kovnir, K. A.; Sobolev, A. V.; Presniakov, I. A.; Prots, Y.; Baitinger, M.; W, S.; Olenev, A. V.; Lebedev, O. I.; Tendeloo, G. V.; Grin, Y.; Shevelkov, A. V. *Chem. Eur. J.* **2007**, *13*, 5090–5099.
(54) von Schnering, H.-G. *Nova Acta Leopoldina* **1985**, *59*, 168.
(55) Beekman, M.; Nolas, G. S. *Int. J. Appl. Ceram. Tech.* **2007**, *4*, 332–338.
(56) Carrillo-Cabrera, W.; Budnyk, S.; Prots, Y.; Grin, Y. *Z. Anorg. Allg. Chem.* **2004**, *630*, 2267–2276.
(57) Okamoto, N. L.; Tanaka, K.; Inui, H. *Acta Mater.* **2006**, *54*, 173–178.
(58) Melnychenko-Koblyuk, N.; Grytsiv, A.; Berger, S.; Kaldarar, H.; Michor, H.; Rohrbacher, F.; Royanian, E.; Bauer, E.; Rogl, P.; H. Schmid Giester, G. *J. Phys. Cond. Matter* **2007**, *19*, 046203.
(59) Melnychenko-Koblyuk, N.; Grytsiv, A.; Rogl, P.; Rotter, M.; Lackner, R.; Bauer, E.; Fornasari, L.; Marabelli, F.; Giester, G. *Phys. Rev. B* **2007**, *76*, 195124.
(60) Chasmar, R. P.; Stratton, R. *J. Electron. Control* **1959**, *7*, 52.
(61) Fistul, V. I. *Heavily Doped Semiconductors*; Plenum Press: New York, 1969.
(62) Slack, G. A.; Tsoukala, V. G. *J. Appl. Phys.* **1994**, *76*, 1665–1671.
(63) Snyder, G. J.; Caillat, T.; Fleurial, J.-P. *Phys. Rev. B* **2000**, *62*, 10185.
(64) Anno, H.; Kawamura, M. H. M.; Nanao, J. Matsubara, K. 22st International Conference on Thermoelectronics, **2003**; pp 121−126.
(65) Blake, N. P.; Latturner, S.; Bryan, J. D.; Stucky, G. D.; Metiu, H. *J. Chem. Phys.* **2001**, *115*, 8060.
(66) Johnsen, S.; Bentien, A.; Madsen, G. K. H.; Nygren, M.; Iversen, B. B. *Phys. Rev. B* **2007**, *76*, 245126.
(67) Anno, H.; Hokazono, M.; Kawamura, M.; Matsubara, K. Effect of transition element substitution on thermoelectric properties of semiconductor clathrate compounds. *Proceedings of ICT 2003, The Twenty-Second International Conference on Thermoelectrics*, La Grande-Motte, France, Aug 17−21, **2003**; pp 121−126.
(68) Martin, J.; Erickson, S.; Nolas, G. S.; Alboni, P.; Tritt, T. M.; Yang, J. *J. Appl. Phys.* **2006**, *99*, 044903.
(69) Okamoto, N. L.; Kishida, K.; Tanaka, K.; Inui, H. *J. Appl. Phys.* **2007**, *101*, 113525.
(70) Tang, X.; Li, P.; Deng, S.; Zhang, Q. *J. Appl. Phys.* **2008**, *104*, 013706.
(71) Deng, S.; Tang, X.; Li, P.; Zhang, Q. *J. Appl. Phys.* **2008**, *103*, 073503.
(72) Sasaki, Y.; Kishimoto, K.; Koyanagi, T.; Asada, H.; Akai, K. *J. Appl. Phys.* **2009**, *105*, 073702.
(73) Madsen, G. K. H.; Schwarz, K.; Blaha, P.; Singh, D. J. *Phys. Rev. B* **2003**, *68*, 125212.
(74) Tang, J.; Rachi, T.; Kumashiro, R.; Avila, M. A.; Suekuni, K.; Takabatake, T.; Guo, F. Z.; Akai, K. K. K.; Tanigaki, K. *Phys. Rev. B* **2008**, *78*, 085203.
(75) Mudryk, Y.; Rogl, P.; Paul, C.; Berger, S.; Bauer, E.; Hilscher, G.; Godart, C.; Noel, H. *J. Phys.: Condens. Matter* **2002**, *14*, 7991–8004.
(76) Eto, T.; Kishimoto, K.; Koga, K.; Akai, K.; Koyanagi, T.; Anno, H.; Tanaka, T.; Kurisu, H.; Yamamoto, S.; Matsuura, M. *Mater. Trans.* **2009**, *50*, 631–639.
(77) Hokazono, M.; Kawamura, M.; Anno, H.; Matsubara, K. *Trans. Mater. Res. Soc. Jpn.* **2004**, *29*, 2793.
(78) Anno, H.; Hokazono, M.; Takakura, H.; Matsubara, K. International Conference on Thermoelectrics, **2005**; p 102.
(79) Cordier, G.; Wol, P. *J. Less-Common Met.* **1991**, *169*, 291.
(80) Hokazono, M.; Anno, H.; Matsubara, K. *Mater. Trans.* **2005**, *46*, 1485–1489.
(81) Anno, H.; Hokazono, M.; Takakura, H.; Matsubara, K. Thermoelectric properties of $Ba_xAu_xGe_{46-x}$ clathrate compounds. *Proceedings of ICT 2005, The Twenty-Fourth International Conference on Thermoelectrics*, Clemson, SC, June 19−23, **2005**; pp 102−105.
(82) Caillat, T.; Borshchevsky, A.; Fleurial, J.-P. *J. Appl. Phys.* **1996**, *80*, 4442–4449.
(83) Dyck, J. S.; Chen, W.; Uher, C.; Chen, L.; Tang, X.; Hirai, T. *J. Appl. Phys.* **2002**, *91*, 3698–3705.

(84) Kuznetsov, V. L.; Kuznetsova, L. A.; Rowe, D. M. *J. Phys.: Cond. Matter* **2003**, *15*, 5035–5048.
(85) Zhao, X. Y.; Shi, X.; Chen, L. D.; Zhang, W. Q.; Zhang, W. B.; Pei, Y. Z. *J. Appl. Phys.* **2006**, *99*, 053711.
(86) Bai, S.; Pei, Y.; Chen, L.; Zhang, W.; Zhao, X.; Yang, J. *Acta Mater.* **2009**, *57*, 3135–3139.
(87) Singh, D.; Pickett, W. *Phys. Rev. B* **1994**, *50*, 11235–11238.
(88) Singh, D. J.; Mazin, I. I. *Phys. Rev. B* **1997**, *56*, R1650.
(89) May, A. F.; Singh, D. J.; Snyder, G. J. *Phys. Rev. B* **2009**, *79*, 153101.
(90) Fisher, I. R.; Wiener, T. A.; Bud'ko, S. L.; Canfield, P. C.; Chan, J. Y.; Kauzlarich, S. M. *Phys. Rev. B* **1999**, *59*, 13829–13834.
(91) Fisher, I. R.; Budko, S. L.; Song, C.; Canfield, P. C.; Ozawa, T. C.; Kauzlarich, S. *Phys. Rev. Lett.* **2000**, *85*, 1120–1123.
(92) Madsen, G. K. H. *J. Am. Chem. Soc.* **2006**, *128*, 12140–12146.
(93) Xu, J.; Kleinke, H. *J. Comput. Chem.* **2008**, *29*, 2134–2143.
(94) Minnich, A. J.; Dresselhaus, M. S.; Ren, Z. F.; Chen, G. *Energy Environ. Sci.* **2009**, *2*, 466–479.
(95) Medlin, D. L.; Snyder, G. J. *Curr. Opin. Colloid Interface Sci.* **2009**, *14*, 226–235.
(96) Klemens, P. G. *Phys. Rev.* **1960**, *119*, 507–509.
(97) Callaway, J.; von Baeyer, H. C. *Phys. Rev.* **1960**, *120*, 1149–1154.
(98) Abeles, B. *Phys. Rev.* **1963**, *131*, 1906–1911.
(99) Yang, J.; Meisner, G. P.; Chen, L. *Appl. Phys. Lett.* **2004**, *85*, 1140–1142.
(100) Meisner, G. P.; Morelli, D. T.; Hu, S.; Yang, J.; Uher, C. *Phys. Rev. Lett.* **1998**, *80*, 3551–3554.
(101) Zaikina, J. V.; Schnelle, W.; Kovnir, K. A.; Olenev, A. V.; Grin, Y.; Shevelkov, A. V. *Sol. State Sci.* **2007**, *9*, 664–671.
(102) Toberer, E. S.; May, A. F.; Melot, B.; Flange-Larsen, E.; Snyder, G. J. Dalton Trans., in press.
(103) Keppens, V.; Mandrus, D.; Sales, B.; Chakoumakos, B.; Dai, P.; Coldea, R.; Maple, M.; Gajewski, D.; Freeman, E.; Bennington, S. *Nature* **1998**, *395*, 876–878.
(104) Koza, M. M.; Johnson, M. R.; Viennois, R.; Mutka, H.; Girard, L.; Ravot, D. *Nat. Mater.* **2008**, *7*, 805–810.
(105) Wang, Y.; Xu, X.; Yang, J. *Phys. Rev. Lett.* **2009**, *102*, 175508.
(106) Yang, J.; Zhang, W.; Bai, S. Q.; Mei, Z.; Chen, L. D. *Appl. Phys. Lett.* **2007**, *90*, 192111.
(107) Shi, X.; Kong, H.; Li, C.-P.; Uher, C.; Yang, J.; Salvador, J. R.; Wang, H.; Chen, L.; Zhang, W. *Appl. Phys. Lett.* **2008**, *92*, 182101.
(108) Cohn, J. L.; Nolas, G. S.; Fessatidis, V.; Metcalf, T. H.; Slack, G. A. *Phys. Rev. Lett.* **1999**, *82*, 779.
(109) Bentien, A.; Johnsen, S.; Iversen, B. B. *Phys. Rev. B* **2006**, *73*, 094301.
(110) Yi, T.; Toberer, E. S.; Cox, C. A.; Kauzlarich, S. M.; Snyder, G. J. Chem. Mater., in press.
(111) Slack, G. A. *Solid State Physics*; Academic Press: New York, 1979; Vol. *34*.
(112) Patschke, R.; Zhang, X.; Singh, D.; Schindler, J.; Kannewurf, C. R.; Lowhorn, N.; Tritt, T.; Nolas, G. S.; Kanatzidis, M. G. *Chem. Mater.* **2001**, *13*, 613–621.
(113) Assoud, A.; Thomas, S.; Sutherland, B.; Zhang, H.; Tritt, T. M.; Kleinke, H. *Chem. Mater.* **2006**, *18*, 3866–3872.
(114) Hsu, K.-F.; Chung, D.-Y.; Lal, S.; Mrotzek, A.; Kyratsi, T.; Hogan, T.; Kanatzidis, M. G. *J. Am. Chem. Soc.* **2002**, *124*, 2410–2411.
(115) Chung, D.-Y.; Hogan, T. P.; Rocci-Lane, M.; Brazis, P.; Ireland, J. R.; Kannewurf, C. R.; Bastea, M.; Uher, C.; Kanatzidis, M. G. *J. Am. Chem. Soc.* **2004**, *126*, 6414–6428.
(116) Chung, D.-Y.; Jobic, S.; Hogan, T.; Kannewurf, C. R.; Brec, R.; Rouxel, J.; Kanatzidis, M. G. *J. Am. Chem. Soc.* **1997**, *119*, 2505–2515.
(117) May, A. F.; Toberer, E. S.; Snyder, G. J. *J. Appl. Phys.* **2009**, *106*, 013706.
(118) Condron, C. L.; Kauzlarich, S. M.; Gascoin, F.; Snyder, G. J. *J. Sol. State Chem.* **2006**, *179*, 2252.
(119) Wang, X.-J.; Tang, M.-B.; Zhao, J.-T.; Chen, H.-H.; Yang, X.-X. *Appl. Phys. Lett.* **2007**, *90*, 232107.
(120) Kim, S.-J.; Ireland, J. R.; Kannewurf, C. R.; Kanatzidis, M. G. *J. Sol. State Chem.* **2000**, *155*, 55–61.
(121) Kim, S.-J.; Hu, S.; Uher, C.; Kanatzidis, M. G. *Chem. Mater.* **1999**, *11*, 3154–3159.